ADVANCED OPTICAL MATERIALS
www.advopticalmat.de

Iontronically Tunable Broadband Graded Index Films

*Paolo Franceschini, Andrea Tognazzi, Virginia Maria Demartis, Luca Carletti, Evgenii Menshikov, Ivano Alessandri, Alfonso Carmelo Cino, Fabrizio Torricelli, Costantino De Angelis, and Maria Antonietta Vincenti**

Tunable optical devices are of paramount importance in modern optical engineering, offering the flexibility to dynamically adjust key optical parameters, thus enhancing functionality and adaptability. In this study, a fresh approach is presented to achieve on-demand, spatially tunable optical properties using organic mixed ion-electron conductors, which can be produced using large-scale, cost-effective technologies. It is demonstrated how, by exploiting, the spatial modulation of the bulk electronic conductance of PEDOT:PSS through an organic electrochemical transistor configuration, we can create a spatially tunable broadband gradient index profile with multiple degrees of freedom. These findings introduce a new class of tunable graded index media, which hold potential for a wide range of applications that span from optical interconnections to multi-focal optical devices.

1. Introduction

The quest for novel materials that can seamlessly blend high electrical conductivity, optical transparency, mechanical flexibility, thermal stability and ease of manufacturing has gradually led, over the last decades, to indicate Poly(3,4-ethylenedioxythiophene) polystyrene sulfonate (PEDOT:PSS) as the perfect candidate for the job. This polymer composite, consisting of PEDOT (a conjugated polymer) and PSS (a polyelectrolyte), has in fact emerged as a versatile platform for various applications. Owing to its combined transparency and adjustable work function, PEDOT:PSS is now widely integrated in transparent electrodes,[1–3] which are crucial for the performance and aesthetic of optoelectronic devices,[4] as well as for organic light-emitting diodes, organic photovoltaics, electrochromic devices, and sensors.[5,6] In the broader area of organic electronics, PEDOT:PSS's role extends also to flexible displays, wearable electronics, and bioelectronic devices.[7] Its ease of processing from aqueous dispersion allows in fact for cost-effective manufacturing through large-area high-throughput fabrication techniques, therefore showing a significant advantage over traditional inorganic transparent conductors like indium tin oxide.[8] The biocompatibility of PEDOT:PSS makes it also an excellent candidate for biomedical devices, such as neural interfaces and biosensors.[9] One of the most compelling aspects of PEDOT:PSS is its tunability over a wide set of parameters. By varying the ratio of PEDOT to PSS or by incorporating secondary dopants, the electrical, optical, and mechanical properties of PEDOT:PSS can be finely adjusted to meet specific application requirements.[10,11] PEDOT:PSS conductivity can also be modulated by injecting mobile ionic species originating from an adjacent electrolyte.[12] While all approaches are valuable in terms of degree of tunability, the latter has been proven to be promising also for the realization of reconfigurable optical devices operating at the nanoscale level. PEDOT:PSS can be, for example, used as the control layer of a plasmonic metasurface to achieve dynamic beam steering,[13] it can be exploited to realize tunable Mie[14] or plasmonic[15] resonators, or, when properly patterned, it can be arranged itself in a form of metasurface acting as a dynamically tunable metadevice.[16,17] Although the modulation of the optical properties shown in refs. [13–17] is remarkable and allows to realize a number of functionalities without recurring to the use of nematic or phase-change materials (see ref. [18] and references therein), the proposed devices are severely limited in terms of modulation of their properties within their volume. In other words, all proposed configurations only allow for a homogeneous variation of the PEDOT:PSS' refractive index so that their operation reduces to a mere on/off regime even when stacked or combined in a different fashion.[14] Optical and electrical properties of PEDOT:PSS and its tunability in the infrared and visible

P. Franceschini, V. M. Demartis, L. Carletti, E. Menshikov, I. Alessandri, F. Torricelli, C. De Angelis, M. A. Vincenti
Università degli studi di Brescia
Via Branze 38, Brescia 25123, Italy
E-mail: maria.vincenti@unibs.it

P. Franceschini, A. Tognazzi, L. Carletti, C. De Angelis, M. A. Vincenti
Istituto Nazionale di Ottica - Consiglio Nazionale delle Ricerche (INO-CNR)
Via Branze 45, Brescia 25123, Italy

A. Tognazzi, A. C. Cino
Università degli studi di Palermo
Viale delle Scienze, Palermo 90128, Italy

The ORCID identification number(s) for the author(s) of this article can be found under https://doi.org/10.1002/adom.202402410

DOI: 10.1002/adom.202402410

range have been, in fact, characterized only when its properties are set at the fabrication stage[19–23] or when the polymer acts as a capacitor.[13,24,25] However, a more effective approach to develop both bulk and planar optical devices would require the realization of a gradient index profile within the volume of a film or a nanostructure, namely the realization of a gradient index metasurface or metamaterial.[26] Those engineered nanostructures can, in fact, manipulate electromagnetic waves in ways that go beyond what traditional materials can achieve, lending themselves for applications that span from chromatic aberration correction, to beam steering, holography, sensing and quantum optics, to name a few.[18,27] At the same time, developing an optical platform whose graded index (GRIN) profile can be tuned on demand could significantly expand the applications of graded index optics while, at the same time, lower the cost of fabrication of those materials.

Here, we demonstrate that a spatially controlled refractive index profile can be realized in a PEDOT:PSS film by exploiting a three-terminal organic electrochemical transistor (OECT) configuration. More specifically, by properly applying gate and drain voltages, we are able to inject the ions into the polymer in a well controlled fashion, leading to a spatial distribution of charge concentration along the polymer length. The interaction between bulk ionic and electronic charges results in a spatially tunable gradient index that can be extracted from transmission measurements through a thin film of PEDOT:PSS. By modeling the (complex) refractive index of the medium with a combination of Drude and Lorentz oscillators, we are able to determine the spatial variation of plasma frequencies, damping and resonance frequency at each point in the polymer film and for three different connection schemes. Our results reveal that different drain and/or gate voltage configurations lead to different modulation over the PEDOT:PSS film, therefore providing a very broad set of combination for refractive index tuning across the volume of the polymer. Our results show that the injection of external carriers, namely ions, modifies the electrical properties of PEDOT:PSS over a broadband range, demonstrating a practical path to overcome the limitations of currently available GRIN materials[28–30] while potentially providing the same functionalities and features.[31,32] The voltage-programmable ionic modulation offers an unprecedented degree of spatio-optical tunability, crucial for the development and engineering of GRIN photonic devices realized without requiring any nanoscale patterning. The proposed solution also circumvents blazed grating effects that can result from the periodic repetition of optical elements. The refractive index modulation achieved along the PEDOT:PSS film shows that by simply exploiting different connection schemes one can realize tunable axial and radial profiles with isoindices surfaces that are controlled through the voltage applied across the structure. In other words, the extreme degree of freedom provided by the proposed platform let us envision the possibility to develop a completely novel class of flat, ultra-compact, broadband optical devices, including adaptable optical interconnections, tunable focal length devices,[16] low-frequency displays[15] or smart windows.[33] All these devices find a crucial role in various fields, including telecommunications, medicine, astronomy, defense, and surveillance.

2. Results and Discussion

A layer of conductive polymer PEDOT:PSS was deposited by spin coating technique. This method was chosen due to its simplicity and its ability to achieve uniform and precisely controlled film thickness. The morphology and thickness (750 nm) of the deposited film were analyzed using atomic force microscopy, with results presented in **Figure 1a** (inset) and Figure S1 (Supporting Information).

The deposited film has been optically characterized by measuring its linear transmittance in the visible-near-infrared (VIS-NIR, 500–1600 nm wavelength) spectral range (see Experimental Section for additional details). In Figure 1a, we show the measured transmittance spectrum (light blue solid line) of the 750-nm-thick PEDOT:PSS film (T_F). The experimental transmittance spectrum can be reproduced by a theoretical profile (black solid line in Figure 1a based on the Transfer Matrix Method[34] and the Drude–Lorentz model of the material refractive index $\hat{N}$, which is related to the dielectric function (ε) as $\varepsilon = \hat{N}^2 = (n + ik)^2$[35] (with n and k being the real and imaginary part, respectively).

In particular, in the spectral region of interest, the refractive index can be assumed as

$\hat{N}^2(\lambda) = \hat{N}_\infty^2 + \hat{N}_D^2(\lambda) + \sum_q \hat{N}_{Lq}^2(\lambda)$, i.e., the sum of a Drude oscillator term $\hat{N}_D^2$, several Lorentz terms $\hat{N}_{Lq}^2$ (indexed by q), and a constant $\hat{N}_\infty^2$, which describe intraband, interband, and high-energy interband transitions, respectively (see Experimental Section for additional details). The refractive index spectral profile resulting from the analysis is displayed in Figure 1b and Figure 1c (n and k, respectively), where the total profiles (thick solid line) are shown together with the contributions ascribed to the various transitions (color areas), see Section S5 (Supporting Information) for more details. The Drude component with plasma frequency $\omega_D = 1.166$ rad/fs ($\lambda_p = 2\pi c/\omega_D = 1615.5$ nm) dominates the spectrum above 1300 nm (light-blue-colored patterned area in Figure 1b), while the shorter wavelength region is characterized by the presence of Lorentz oscillators (yellow-colored patterned area in Figure 1b) ascribed to excitations of polaron and bipolaron states.[20,25,36,37] We then proceed to evaluate the changes of the optical properties of PEDOT:PSS by adopting a three electrode configuration that provides the desired electrical tuning[38] (see **Figure 2a**). The film and the electrodes are enclosed in an electrochemical cell filled with an ionic medium. In this arrangement, the overall device behaves as an OECT, as shown by the circuit displayed in Figure 2a. Further details on the device fabrication and electrical connection scheme are provided in the Experimental Section.

Typical transfer and output characteristics of the fabricated devices are depicted in Figure 2b,c, respectively. In the case of PEDOT:PSS OECTs, the channel is made of a polymer blending composed of a PSS-rich matrix hosting nano-metric sized PEDOT-rich grains. The electronic (hole) conduction takes place in the PEDOT while ionic conduction is provided by the PSS polyelectrolyte. The fixed negative charges into the poly-electrolyte (N_{fix}) are compensated by mobile cations provided by the electrolyte while N_{fix} at the PSS/PEDOT interface are compensated by electronic charges (holes).[39] This ionic-electronic interaction results in an intrinsic doping concentration, providing p-type

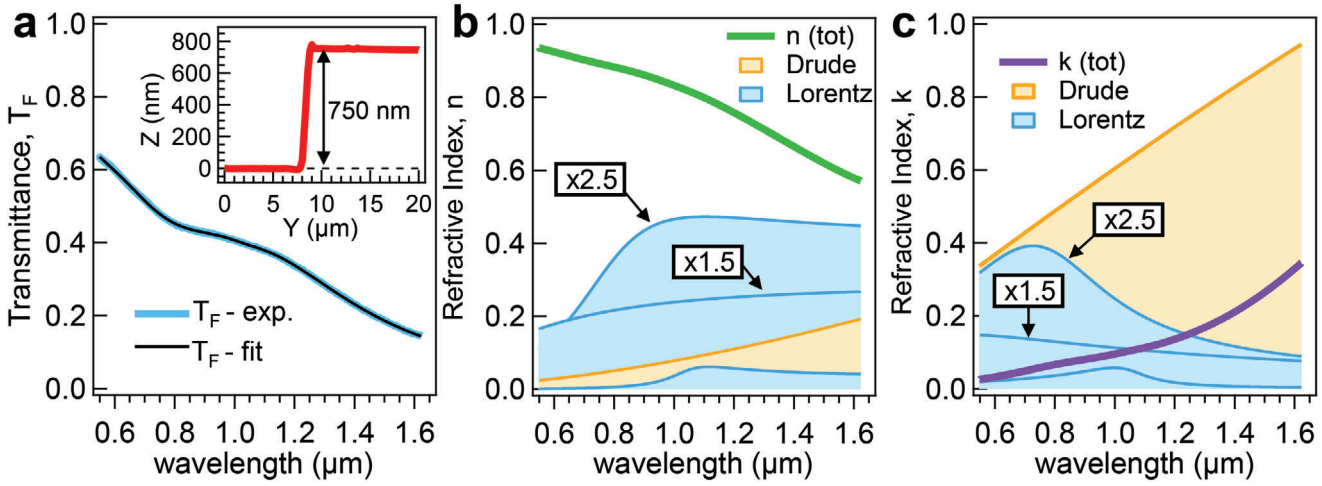

Figure 1. PEDOT:PSS Film Optical Properties. a) Broadband transmittance spectrum of the fabricated PEDOT:PSS film measured in the visible and near infra-red spectral range (blue solid line). A theoretical model based on Drude-Lorentz oscillators (black solid line) has been fitted to the data. The inset shows the output of the profilometer analysis. b,c) Refractive index profile, real part *n* (b, thick green line) and imaginary part *k* (c, thick violet line), resulting from the fit of the data in panel a together with the individual contributions of the intraband (Drude, yellow shaded area) and interband (Lorentz, light blue shaded areas) oscillators. The value of the parameters resulting from the fit are reported in the Supporting Information.

normally-on OECTs. The direct visualization of voltage-induced migration of cations and anions within the polymer (with particular focus on the time-resolved propagation of the dedpoing front) extensively investigated in refs. [40–43]. On the other hand, the proposed three-electrode configuration provides additional degrees of freedom in terms of charge modulation, since the electronic current flowing from source to drain (I_D) can be modulated by the concentration of mobile cations or anions injected and accumulated into the polymer. When a positive gate voltage (V_G) is applied, cations drift into the polymer, reducing the hole concentration and decreasing the drain current (I_D). Conversely, applying a negative V_G causes previously injected cations to drift

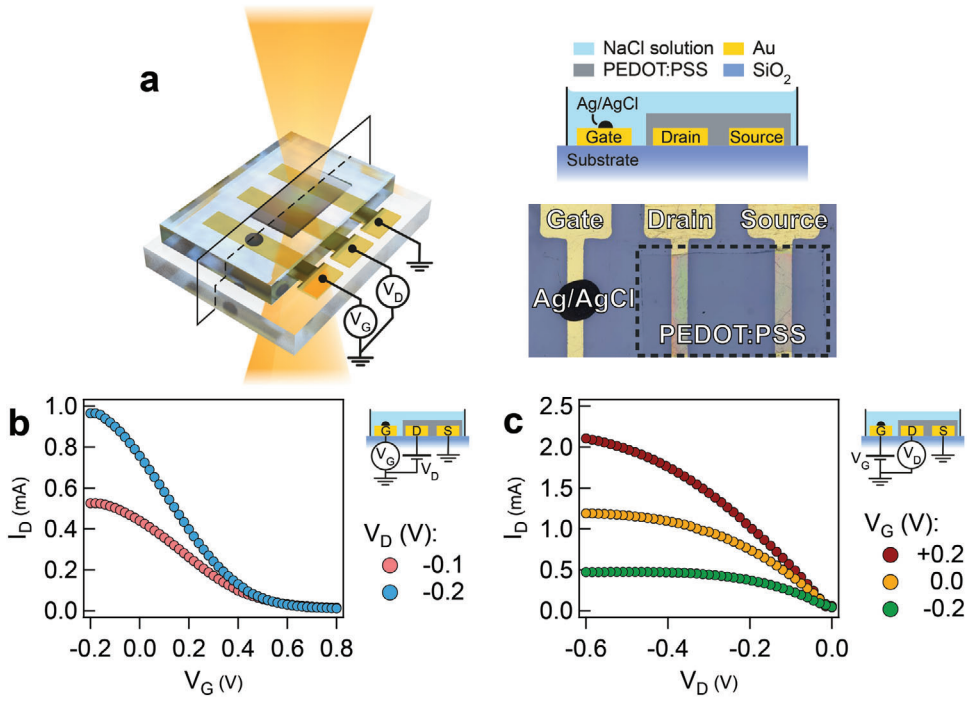

Figure 2. Electronic Properties of the Device. a) Sketch of the fabricated device. G: gate electrode; D: drain electrode; S: source electrode. The lateral gate (black dot) is a non-polarizable Ag/AgCl printed electrode. The right-top image sketches the cross-section of the device. The right-bottom image displays a picture (top view) of the fabricated device (with the black dashed line outlining the PEDOT:PSS film). b) Transfer characteristics I_D-V_G (drain current *vs* gate voltage) for various drain voltage levels V_D. c) Output characteristics I_D-V_D (drain current *vs* drain voltage) for various gate voltage levels V_G. b,c) The schemes on the right side represent the layout of the electronic circuit.

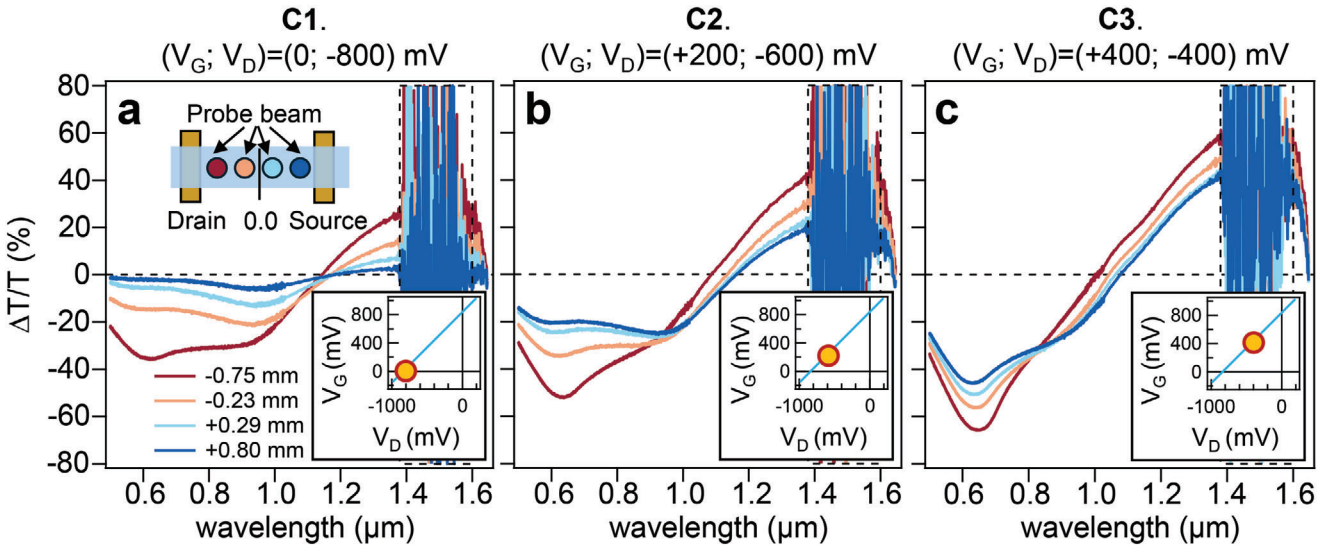

Figure 3. Space-resolved Relative Transmittance Variation of the Device. $\Delta T/T$ spectra measured for three voltage configuration: (V_G, V_D) = (0, −800) mV (a), (V_G, V_D) = (+200, −600) mV (b), and (V_G, V_D) = (+400, −400) mV (c). In each panel spectra at various position (defined with respect to the center of the channel) within the drain-source channel are displayed: –0.75 mm (dark red trace, near drain electrode), –0.23 mm (pink), +0.29 mm (light blue), and +0.80 mm (dark blue, near source electrode). The inset in panel a (top-left) shows a sketch of the space-resolved approach. The insets (bottom-right) display schematically the position of each configuration in the $V_G - V_D$ plane. The dashed black line (1400–1600 nm) denotes the spectral range where $\Delta T/T$ spectra are noisy due to strong light absorption (*very low transmittance*) occurring in the ionic liquid component (see Figure S3 (Supporting Information) for more details), thus hindering the relative variation signal from the PEDOT:PSS film.

out of the polymer, while anions drift into the polymer. This process increases the hole concentration, resulting in a larger I_D. Therefore, the spatial distribution of hole concentration along the channel depends on the applied voltages. Specifically, when the OECT operates at small drain voltages (Figure 2c) the current linearly increases with V_D and an almost uniform distribution of charge carriers along the channel results in an equivalent linear resistance. This linear condition results in a linear increase of the drain current with the applied V_D. By increasing V_D to more negative voltages, cations are extracted and anions are accumulated at the drain side of the channel. The hole concentration in the semiconductor phase (PEDOT) decreases with increasing anion concentration and a pinch-off of the channel is obtained. This gives rise to a saturation of the I_D characteristics and to a non-uniform charge distribution along the PEDOT:PSS channel. A good example of this operating regime is shown in Figure 2c where V_D < −0.4 V and V_G = 0.2 V and the current is almost independent of V_D.

To probe the carrier concentration variation within the PEDOT:PSS film upon external voltage (V_G or V_D) application, we perform space-resolved broadband linear spectroscopy experiments. We measure the relative transmittance variation $\Delta T/T$ defined as the difference between the transmitted light spectra with and without the applied voltage normalized to the transmitted light spectrum without bias applied (see Experimental Section for more details).

Figure 3 displays the measured $\Delta T/T$ spectra for three configurations of the gate (V_G) and drain (V_D) voltages: (V_G, V_D) = (0, −800) mV in panel a (configuration C1), (V_G, V_D) = (+200, −600) mV in panel b (configuration C2), and (V_G, V_D) = (+400, −400) mV in panel c (configuration C3). In these experiments, the gate-drain voltage is kept constant ($V_G - V_D$ = +800 mV) while the gate-source and source-drain voltages are varied simultaneously. As shown in the inset in Figure 3a, for each voltage configuration, the $\Delta T/T$ spectrum has been measured in four different positions across the source-drain channel of the device. The experimental data in Figure 3 clearly show that the $\Delta T/T$ profile spatially changes within the source-drain channel, thus revealing the spatial tunability of the device optical properties. More specifically, it can be seen that, at fixed wavelength, the $\Delta T/T$ signal varies monotonically. Moreover, $\Delta T/T$ spectrum is negative (decreasing transmittance) below 1000 nm, while it becomes positive (increasing transmittance) at longer wavelength, i.e., the spectral region dominated by the Drude component. Moving from the C1 (Figure 3a) to the C3 (Figure 3c) configuration (with decreasing V_D value), the dispersion of the $\Delta T/T$ signal (at fixed λ value) decreases. This result is consistent with the fact that V_D is the parameter responsible for the spatial distribution of carriers within the channel. Therefore, the larger (absolute) V_D value, the more intense the spatial carrier concentration gradient; thus, the larger the dispersion in the transmittance modulation $\Delta T/T$.

The structured variation of transmittance displayed in Figure 3 can be reproduced by assuming a modification of the PEDOT:PSS refractive index (which corresponds to a variation of the Drude-Lorentz oscillator parameters), as discussed more in detail in the Experimental Section. To unravel the modulation of transmittance across the channel, we fitted a theoretical curve, $\Delta T/T = T_{F,V}/T_F - 1$, to the experimental data in Figures 3A-C (see Experimental Section for additional details). Here, the $T_{F,V}$ term, describing the film transmittance spectrum upon voltage application, has been calculated by varying the values of the Drude–Lorentz oscillators parameters previously determined to reproduce T_F. We underline that in our approach (similar to the one

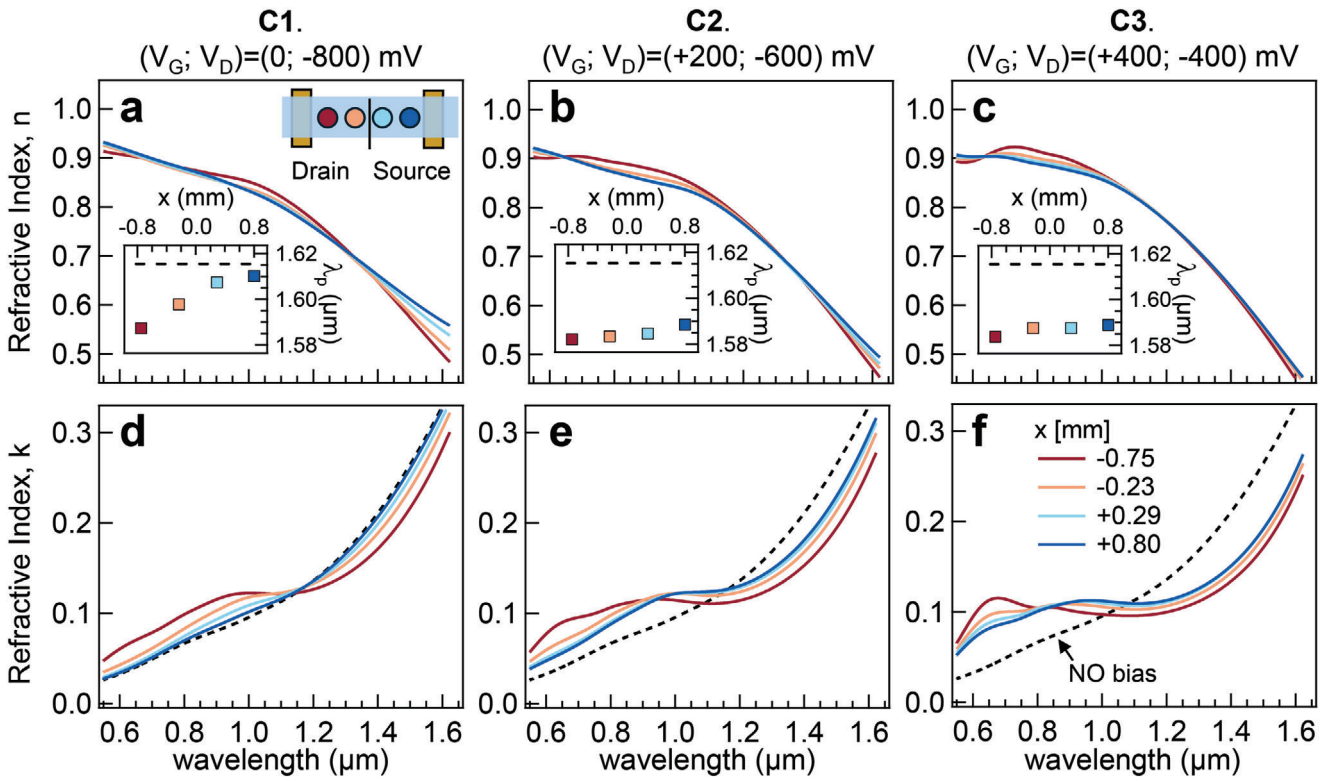

Figure 4. Voltage-Induced Modulation of the Refractive Index. Space-resolved refractive index $n + ik$, real (a–c) and imaginary part (d–f), resulting from the differential analysis of the data in Figure 3. The inset in panel a (top-right) denotes the four positions, within the source-drain channel, where the spectra have been measured: −0.75 mm (dark red trace, near drain electrode), −0.23 mm (pink), +0.29 mm (light blue), and +0.80 mm (dark blue, near source electrode). a and d, (V_G, V_D) = (0, −800) mV; b and e, (V_G, V_D) = (+200, −600) mV; c and f, (V_G, V_D) = (+400, −400) mV. a–c) The insets (bottom-left) report the value of λ_p ($\tilde{} = \tilde{}2\pi\hbar c/\omega_D$) parameter used to calculate the corresponding refractive index profile (the dashed black line highlights the value of λ_p) in absence of bias. d–f) The dashed dotted black line indicates the refractive index (imaginary part) in absence of bias.

in Ref. [44]), the theoretical $\Delta T/T$ model satisfies the Kramers–Kronig relations since the individual models $T_{F,V}$ and T_F are Kramers–Kronig consistent. The results of the analysis are displayed in **Figure 4** in terms of refractive index, real part (*n*, panels A-C) and imaginary part (*k*, panels D-F), where the latter exhibits a larger variation. In particular, the data suggest that the application of voltage determines: *i)* a decrease in the spectral weight at longer wavelength (Drude region, IR) accompanied by an increase of spectral weight at lower wavelength (VIS) and *ii)* the amplitude of the variation increases across the channel (from the source to the drain electrode). We note that the larger spatial gradient of the dielectric function across the source-drain channel occurs for the (V_G, V_D) = (0, −800) mV configuration (labeled C1 in Figure 4). If we now focus our attention on the Drude component of the dielectric function, the differential analysis reveals that, upon voltage application, the value of the plasma frequency ω_D (damping coefficient γ_D) is higher (lower) than that in absence of bias near the source electrode, as reported in **Table 1**; moreover, ω_D (γ_D) further increases (decreases) moving towards the drain electrode. These behaviors align with the observation that increasing the gate voltage decreases the hole concentration in the bulk of PEDOT, while lowering the drain voltage enhances the non-uniform charge spatial distribution along the polymer from source to drain. As a reference, the spatial modulation of the Drude plasma frequency is reported in the insets of Figure 4D–F in terms of λ_p (= $2\pi\hbar c/\omega_D$). We note that, for the (V_G, V_D) = (0, −800) mV configuration (C1), a 28-nm blue-shift of λ_p is achieved.

Our results demonstrate the occurrence of a bias-induced spatial gradient of the refractive index, which we envision as a key element for a novel class of GRIN platforms. Indeed, the voltage-induced modulation of the dielectric function across the PEDOT:PSS channel (see Figure 4) allows to infer what is the expected phase accumulation for a plane wave that traverses the film. Since the OECT configuration induces a change in the bulk properties of the material that depends on the applied voltage but it is completely independent on the film thickness, we can vary the PEDOT:PSS layer to obtain a specific phase accumulation. To give a sense of the degrees of freedom offered by the proposed platform in terms of both tunability and range of functionality, we calculated the phase accumulation difference across the PEDOT:PSS channel, namely the phase difference between the red dot and the dark blue dot in the inset of Figure 3. This estimation provides a value of the refractive index gradient across the electrode gap (i.e., a global rather than local value). The calculation was repeated for several thicknesses and for the three connection schemes C1, C2, and C3. **Figure 5** shows that, since the modulation of the dielectric function in those three configurations is quite strong, the phase accumulation difference between the extremes of the PEDOT:PSS channel can vary between

Table 1. Drude Oscillator Parameters. Oscillator parameters of the Drude term of the refractive index: ω_D (plasma frequency), γ_D (damping coefficient), and $\lambda_p = 2\pi c/\omega_D$. Top part: parameters retrieved in the case where no bias is applied to the device (Figure 1). Bottom part: parameters retrieved for the three voltage configurations analyzed (Figures 3 and 4). [D]: drain electrode; [S]: source electrode.

$[V_G, V_D]$	[0,0] mV		
	λ_p [nm]	ω_D [rad/fs]	γ_D [rad/fs]
	1615.5	1.166	0.493

(V_G, V_D)	(0, −800) mV			(+200, −600) mV			(+400, −400) mV		
x [mm]	λ_p [nm]	ω_D [rad/fs]	γ_D [rad/fs]	λ_p [nm]	ω_D [rad/fs]	γ_D [rad/fs]	λ_p [nm]	ω_D [rad/fs]	γ_D [rad/fs]
−0.75 [D]	1587.4	1.187	0.292	1582.1	1.191	0.240	1583.7	1.189	0.198
−0.23	1597.7	1.179	0.342	1583.3	1.190	0.282	1587.5	1.187	0.223
+0.29	1607.4	1.172	0.412	1584.6	1.189	0.306	1587.5	1.187	0.239
+0.80 [S]	1610.2	1.170	0.466	1588.5	1.186	0.329	1588.9	1.186	0.239

tenths of degrees for a 500 nm film in configuration C3 to approximately 360 degrees for a 20 µm film in configuration C1. Such tunability is especially pronounced in the NIR, where the modulation of the dielectric permittivity is stronger. We stress that the proposed approach can be easily extended to other materials belonging to the class of organic mixed ionic–electronic conductors (OMIECs),[45–47] which are all based on the combination of a conjugated polymer (i.e., the active layer) and an electrolyte (i.e., ionic conductor in liquid, gel,[48–50] or solid form). In OMIECs the choice of the polymer determines the nature of the charge carriers (p- or n-type) and the operational mode (depletion or enhancement) of the device. For example we identify as an alternative to PEDOT:PSS (p-type and operating in depletion mode), the material P(g2T-TT).[51] Other possibilities of p-type enhancement operational mode are P3CPT or PgBTTT,[52] while alternative n-type polymers are PBFDO, BBL[53] or BBL:PEI,[54] which both operate in depletion mode. Finally, p(gDPP-V) might also be a good candidate for single-component ambipolar (p/n-type) devices.[55] In a wider perspective, when considering 2D materials (e.g., graphene or TMDs)[56] as possible alternatives to polymers, care should be exercised because of the limited number of layers composing those materials, therefore hindering their performances. Such performance reduction can be ascribed to the absence of ion penetration within the material thickness, thus remaining only an interfacial mechanism with reduced effect. Indeed, as mentioned in the pioneering work by Bernards and Malliaras,[57] the key characteristics of OMIECs relies on a volumetric response due to the ion penetration into the transistor channel.

3. Conclusion

We demonstrated how to overcome one of the main limitations of GRIN materials, namely the lack of tunability of the refractive index profile after fabrication, by using a voltage-programmable

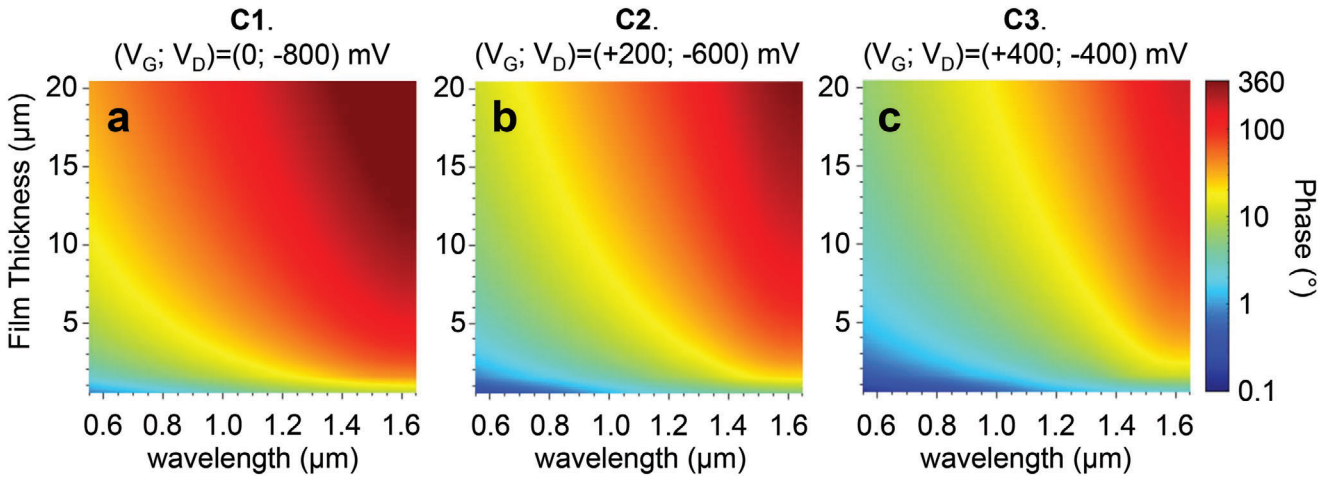

Figure 5. Phase Accumulation Difference. Calculated phase accumulation differences (in degrees) in PEDOT:PSS thin films of various thicknesses in three different connection schemes. a) C1 - (V_G, V_D) = (0, −800) mV; b) C2 - (V_G, V_D) = (+200, −600) mV. c) C3 - (V_G, V_D) = (+400, −400) mV.

ionic modulation of a PEDOT:PSS film connected in a OECT configuration. By judiciously changing the gate and drain voltage we induced different spatial carrier concentration gradients that in turn resulted into different spatial distribution of the optical properties that produce up to 60% transmittance modulation. Our results show that tunable GRIN optics is not only possible, but it can be implemented by using a class of materials, namely OMIECs, that already finds a large use in current electronic technologies. Our findings also suggest that the degrees of freedom offered by the proposed platform in terms of material compositions, electrodes planar distribution and voltage combination allow for the realization of a broad set of flat, ultra-compact and lightweight optical devices whose use can span from optical interconnection and lenses with tunable focal lengths, to collimators and adaptable endoscopic devices, to name a few.

4. Experimental Section

Preparation, Device Fabrication, Electrical and Material Characterization: PEDOT: PSS was mixed with 5%v/v Ethylene Glycol (EG), and 1%v/v ((3-glycidyloxypropyl)- trimethoxysilane) (GOPS). The solution was vigorously mixed for 15 min. 100 nm thick Au source/drain contacts are sputtered through a shadow mask on a glass substrate. Glass substrates were cleaned by sonication in acetone, isopropyl alcohol (IPA), and DI water. They were then dried with nitrogen (N_2) and treated with ozone to promote adhesion of the PEDOT: PSS mix. PEDOT: PSS mix was spin-coated at 1500 rpm for 60 s onto the substrate. Four layers of PEDOT:PSS mix were deposited subsequently, and a soft bake of 1 min at 100°C was performed between the various depositions. A final bake at 140°C for 30 min was performed. A non-polarizable Ag/AgCl gate was deposited near the channel to create the lateral gate, and baked at 120°C for 10 min. A solution of NaCl 100 mM was used as electrolyte.

The DC electrical characteristics were measured with a Keithley 2636 A Source Meter Unit. Transfer characteristics were measured by sweeping the gate voltage, with the source electrode grounded and the drain electrode polarized at a constant potential. The applied gate voltages were varied with a scan rate 80 mV s^{-1}.

Atomic Force Microscopy was performed with Park System Crop NX10, operating in non-contact mode. NSG01 tips by TipsNano were used to record the surface morphology at room temperature and in ambient atmosphere.

Linear Spectroscopy Measurements: To perform linear spectroscopy characterization, we employ an home-built experimental setup similar to the one described in refs. [58, 59]. The source of the broadband probe is given by a stabilized (fiber-coupled) halogen-tungsten lamp (Thorlabs SLS201L), whose output white-light beam is collimated by and a silver parabolic mirror (Thorlabs RC12FC-P01). The electrochemical cell enclosing the device is placed horizontally and its position is controlled by a three-axis stage (manual linear stages, OptoSigma TADC-651S25-M6). By using a pedestal periscope (Thorlabs RS99/M), the probe light propagates vertically and impinges on the sample at normal incidence. A 15-cm focal length lens (Thorlabs LA1433) is employed to focus the beam onto the sample with a spot size (beam waist) $w_0 = (570 \pm 10)$ µm. After the interaction with the sample, the probe beam is collimated by a second lens (Thorlabs LA1433) and sent to the detection stage. The whole spectrum (ranging from 500 to 1600 nm) is measured by two fiber-coupled spectrometers, Andor (500–1000 nm) and NIR-Quest 512-17 (950–1600 nm). A flip mirror after the second lens is employed to route the beam toward the selected spectrometer. The control of voltage level applied to the device has been achieved by using source-meter unit (Keithley 2636 A). The transmittance spectrum T_F of the PEDOT film displayed in Figure 1a is retrieved from a transmittance spectrum of the dry sample T_{dry} (i.e., the condition in which no ionic liquid inside the electrochemical cell) and assuming $T_{dry} = T_F \cdot T_{sub}$, were $T_{sub}(= 0.928 \pm 0.004)$ is the substrate transmittance (constant value across the spectrum). The $\Delta T/T$ profiles displayed in Figure 3 are calculated as $\Delta T/T = \left[T_S^{(V\neq 0)} - T_S^{(V=0)}\right]/T_S^{(V=0)}$, where $T_S^{(V\neq 0)}$ $\left(T_S^{(V=0)}\right)$ is the measured transmittance spectrum of the device (with ionic liquid inside the electrochemical cell) with (without) bias application. See Supporting Information for further details.

Dielectric Function and Transmittance Models: The frequency-dependent dielectric function $\varepsilon = \hat{N}^2$ of the PEDOT:PSS in the spectral region of interest has been modeled as

$$\varepsilon(\omega) = \varepsilon_\infty + \varepsilon_D(\omega) + \sum_q \varepsilon_L^{(q)}(\omega), \tag{1}$$

with $\omega = 2\pi c/\lambda$. The Drude term can be described as $\varepsilon_D(\omega) = -\omega_D^2/\left(\omega^2 + i\omega\gamma_D\right)$, where ω_D is the plasma frequency and γ_D is the damping coefficient, and the q-th Lorentz term is assumed as $\varepsilon_L^{(q)}(\omega) = -\omega_{pq}^2/\left(\omega^2 - \omega_{0q}^2 + i\omega\gamma_q\right)$, where ω_{pq} is the plasma frequency, ω_{0q} is the resonance frequency, and γ_q is the damping coefficient. The curve T_F in Figure 1a has been obtained by combining the Matrix Method, the expression of the dielectric function given in Equation (1), and a set of oscillator parameters $\vec{p}_0 = \{\varepsilon_\infty, \omega_D, \gamma_D, \omega_{01}, \omega_{p1}, \gamma_{L1}, \ldots\}$. The profile $T_{F,V}$ has been calculated by combining the Matrix Method, the expression of the dielectric function given in Equation (1), and a set of oscillator parameters $\vec{p}_V = \vec{p}_0 + \vec{\delta p}$, i.e., the value of the q-th oscillator parameter in the applied voltage condition ($p_V^{(q)}$) is given as a variation (by an amount $\delta p^{(q)}$) of the corresponding parameter in absence of bias ($p_0^{(q)}$):

$p_V^{(q)} = p_0^{(q)} + \delta p^{(q)}$ (see Supporting Information for additional details).

The device transmittance spectrum with (without) bias application has been modeled as $T_S^{(V\neq 0)} = T_{F,V} \cdot T_{sub,V} \cdot T_{liquid,V}$ $\left(T_S^{(V=0)} = T_{dry} \cdot T_{liquid} = T_F \cdot T_{sub} \cdot T_{liquid}\right)$, with $T_{liquid,V}$ (T_{liquid}) being the transmittance of the ionic liquid in presence (absence) of bias application. Moreover, we experimentally determined that $T_{liquid,V} = T_{liquid}$ - i.e., no variation occurs in the spectrum of the ionic liquid upon bias application (see Figure S3, Supporting Information) - and, also, $T_{sub,V} = T_{sub}$; therefore, it follows that $\Delta T/T = \left[T_S^{(V\neq 0)} - T_S^{(V=0)}\right]/T_S^{(V=0)} = \left(T_{F,V} - T_F\right)/T_F = T_{F,V}/T_F - 1$.

Supporting Information

Supporting Information is available from the Wiley Online Library or from the author.

Acknowledgements

This work was partially supported by the European Union under the Italian National Recovery and Resilience Plan (NRRP) of Next Generation EU, of partnership on "Telecommunications of the Future" (PE00000001 - program "RESTART"), S2 SUPER – Programmable Networks, Cascade project PRISM - CUP: E13C22001870001 and by the NATO Science for Peace and Security program (Grant no. 5984).

Open access publishing facilitated by Universita degli Studi di Brescia, as part of the Wiley - CRUI-CARE agreement.

Conflict of Interest

The authors declare no conflict of interest.

Data Availability Statement

The data that support the findings of this study are available from the corresponding author upon reasonable request.

Keywords

graded index optics, organic polymers, tunable devices

Received: September 5, 2024
Revised: December 2, 2024
Published online: December 25, 2024

[1] R. H. Friend, R. Gymer, A. Holmes, J. Burroughes, R. Marks, C. Taliani, D. Bradley, D. D. Santos, J.-L. Bredas, M. Lögdlund, W. R. Salaneck, *Nature* **1999**, *397*, 121.
[2] A. Arias, M. Granström, D. Thomas, K. Petritsch, R. Friend, *Phys. Rev. B* **1999**, *60*, 1854.
[3] L. Roman, M. Berggren, O. Inganäs, *Appl. Phys. Lett.* **1999**, *75*, 3557.
[4] Y. H. Kim, C. Sachse, M. L. Machala, C. May, L. Müller-Meskamp, K. Leo, *Adv. Funct. Mater.* **2011**, *21*, 1076.
[5] A. Elschner, S. Kirchmeyer, W. Lovenich, U. Merker, K. Reuter, *PEDOT: principles and applications of an intrinsically conductive polymer*, CRC press, Boca Raton **2010**.
[6] N. Kim, I. Petsagkourakis, S. Chen, M. Berggren, X. Crispin, M. Jonsson, I. Zozoulenko, in J. R. Reynolds, B. C. Thompson, T. A. Skotheim, editors, *Conjugated Polymers - Properties, Processing, and Applications*, CRC Press, Boca Raton **2019**.
[7] X. Fan, W. Nie, H. Tsai, N. Wang, H. Huang, Y. Cheng, R. Wen, L. Ma, F. Yan, Y. Xia, *Adv. Sci.* **2019**, *6*, 1900813.
[8] Y. Xia, K. Sun, J. Ouyang, *Adv. Mater.* **2012**, *24*, 2436.
[9] R. A. Green, R. T. Hassarati, J. A. Goding, S. Baek, N. H. Lovell, P. J. Martens, L. A. Poole-Warren, *Macromol. Biosci.* **2012**, *12*, 494.
[10] J. Ouyang, *Displays* **2013**, *34*, 423.
[11] J. Kim, J. Jung, D. Lee, J. Joo, *Synth. Met.* **2002**, *126*, 311.
[12] F. Torricelli, D. Z. Adrahtas, Z. Bao, M. Berggren, F. Biscarini, A. Bonfiglio, C. A. Bortolotti, C. D. Frisbie, E. Macchia, G. G. Malliaras, I. McCulloch, M. Moser, T.-Q. Nguyen, R. M. Owens, A. Salleo, A. Spanu, L. Torsi, *Nat. Rev. Methods Primers* **2021**, *1*, 66.
[13] J. Ratzsch, J. Karst, J. Fu, M. Ubl, T. Pohl, F. Sterl, C. Malacrida, M. Wieland, B. Reineke, T. Zentgraf, S. Ludwigs, M. Hentschel, H. Giessen, *J. Opt.* **2020**, *22*, 124001.
[14] A. Karki, G. Cincotti, S. Chen, V. Stanishev, V. Darakchieva, C. Wang, M. Fahlman, M. P. Jonsson, *Adv. Mater.* **2022**, *34*, 2107172.
[15] J. Karst, M. Floess, M. Ubl, C. Dingler, C. Malacrida, T. Steinle, S. Ludwigs, M. Hentschel, H. Giessen, *Science* **2021**, *374*, 612.
[16] J. Karst, Y. Lee, M. Floess, M. Ubl, S. Ludwigs, M. Hentschel, H. Giessen, *Nat. Commun.* **2022**, *13*, 7183.
[17] G. E. Bonacchini, F. G. Omenetto, *Nat. Electron.* **2021**, *4*, 424.
[18] A. M. Shaltout, V. M. Shalaev, M. L. Brongersma, *Science* **2019**, *364*, eaat3100.
[19] V. Singh, T. Kumar, *J. Sci.:Adv. Mater. Devices* **2019**, *4*, 538.
[20] M. Kong, M. Garriga, J. S. Reparaz, M. I. Alonso, *ACS Omega* **2022**, *7*, 39429.
[21] J. Zheng, H. A. Almossalami, K. Chen, X. Yu, H. Ye, *J. Appl. Phys.* **2021**, *129*, 103101.
[22] J. Yang, H. A. Almossalami, Z. Wang, K. Wu, C. Wang, K. Sun, Y. M. Yang, H. Ye, *ACS Appl. Mater. Interfaces* **2019**, *11*, 39132.
[23] S. Doshi, D. Ludescher, J. Karst, M. Floess, J. Carlström, B. Li, N. M. Hemed, Y.-S. Duh, N. A. Melosh, M. Hentschel, M. Brongersma, H. Giessen, *Nanophotonics* **2024**, *13*, 2271.
[24] X. Yu, J. Qiu, Q. Hu, K. Chen, J. Zheng, S. Liang, M. Du, H. Ye, *Opt. Express* **2022**, *30*, 43590.
[25] Q. Hu, X. Yu, H. Liu, J. Qiu, W. Tang, S. Liang, L. Li, M. Du, J. Jia, H. Ye, *ACS Photonics* **2023**, *10*, 3612.
[26] Y. Xu, Y. Fu, H. Chen, *Nat. Rev. Mater.* **2016**, *1*, 1.
[27] A. I. Kuznetsov, M. L. Brongersma, J. Yao, M. K. Chen, U. Levy, D. P. Tsai, N. I. Zheludev, A. Faraon, A. Arbabi, N. Yu, D. Chanda, K. B. Crozier, A. V. Kildishev, H. Wang, J. K. W. Yang, J. G. Valentine, P. Genevet, J. A. Fan, O. D. Miller, A. Majumdar, J. E. Fröch, D. Brady, F. Heide, A. Veeraraghavan, N. Engheta, A. Alù, A. Polman, H. A. Atwater, P. Thureja, R. Paniagua-Dominguez, et al., *ACS Photonics* **2024**, *11*, 816.
[28] T. Bååk, *Appl. Opt.* **1982**, *21*, 1069.
[29] Y. Koike, T. Ishigure, E. Nihei, *J. Lightwave Technol.* **1995**, *13*, 1475.
[30] J. Linares, D. Sotelo, A. Lipovskii, V. Zhurihina, D. Tagantsev, J. Turunen, *Opt. Mater.* **2000**, *14*, 145.
[31] S. H. Song, S. Park, C. H. Oh, P. S. Kim, M. H. Cho, Y. S. Kim, *Opt. Lett.* **1998**, *23*, 1025.
[32] C. Gomez-Reino, M. V. Perez, C. Bao, M. T. Flores-Arias, *Laser Photonics Rev.* **2008**, *2*, 203.
[33] T. Gu, H. J. Kim, C. Rivero-Baleine, J. Hu, *Nat. Photonics* **2023**, *17*, 48.
[34] J. Daillant, A. Gibaud, editors, *X-ray and Neutron Reflectivity: Principles and Applications*, Springer, Berlin Heidelberg **2009**.
[35] M. Dressel, G. Grüner, *Electrodynamics of Solids: Optical Properties of Electrons in Matter*, Cambridge University Press, Cambridge **2002**.
[36] J. Yang, H. Almossalami, Z. Wang, K. Wu, C. Wang, K. Sun, Y. M. Yang, H. Ye, *ACS Appl. Mater. Interfaces* **2019**, *11*, 39132.
[37] I. Zozoulenko, A. Singh, S. K. Singh, V. Gueskine, X. Crispin, M. Berggren, *ACS Appl. Polym. Mater.* **2019**, *1*, 83.
[38] R. Granelli, I. Alessandri, P. Gkoupidenis, I. Vassalini, Z. M. Kovács-Vajna, P. W. M. Blom, F. Torricelli, *Small* **2022**, *18*, 2108077.
[39] P. Romele, M. Ghittorelli, Z. M. Kovács-Vajna, F. Torricelli, *Nat. Commun.* **2019**, *10*, 3044.
[40] E. Stavrinidou, P. Leleux, H. Rajaona, D. Khodagholy, J. Rivnay, M. Lindau, S. Sanaur, G. G. Malliaras, *Adv. Mater.* **2013**, *25*, 4488.
[41] D. Lyu, Y. Jin, P. C. M. M. Magusin, S. Sturniolo, E. W. Zhao, S. Yamamoto, S. T. Keene, G. G. Malliaras, C. P. Grey, *Nat. Mater.* **2023**, *22*, 746.
[42] S. T. Keene, J. E. M. Laulainen, R. Pandya, M. Moser, C. Schnedermann, P. A. Midgley, I. McCulloch, A. Rao, G. G. Malliaras, *Nat. Mater.* **2023**, *22*, 1121.
[43] R. Wu, X. Ji, Q. Ma, B. D. Paulsen, J. Tropp, J. Rivnay, *Sci. Adv.* **2024**, *10*, eadn8628.
[44] C. Giannetti, F. Cilento, S. Dal Conte, G. Coslovich, G. Ferrini, H. Molegraaf, M. Raichle, R. Liang, H. Eisaki, M. Greven, A. Damascelli, D. van der Marel, F. Parmigiani, *Nat. Commun.* **2011**, *2*, 353.
[45] E. Zeglio, O. Inganäs, *Adv. Mater.* **2018**, *30*, 1800941.
[46] B. D. Paulsen, K. Tybrandt, E. Stavrinidou, J. Rivnay, *Nat. Mater.* **2020**, *19*, 13.
[47] J. Tropp, D. Meli, J. Rivnay, *Matter* **2023**, *6*, 3132.
[48] A. Alyami, M. Skowrons, K. Perera, B. Lüssem, A. Jákli, *ACS Appl. Mater. Interfaces* **2024**, *16*, 54282.
[49] G. Frusconi, Z. M. Kovács-Vajna, F. Torricelli, *Adv. Mater. Technol.* **2024**, *9*, 2400301.
[50] B. Sun, S. F. Wan Muhamad Hatta, N. Soin, M. F. Z. B. A. Kadir, F. A. Md Rezali, S. N. Aidit, L. Y. Ma, Q. Ma, *ACS Appl. Electron. Mater.* **2024**, *6*, 2336.
[51] P. Belleri, J. Pons i Tarrés, I. McCulloch, P. W. M. Blom, Z. M. Kovács-Vajna, P. Gkoupidenis, F. Torricelli, *Nat. Commun.* **2024**, *15*, 5350.
[52] A. Makhinia, L. Bynens, A. Goossens, J. Deckers, L. Lutsen, K. Vandewal, W. Maes, V. Beni, P. Andersson Ersman, *Adv. Funct. Mater.* **2024**, *34*, 2314857.
[53] P. Romele, P. Gkoupidenis, D. A. Koutsouras, K. Lieberth, Z. M. Kovács-Vajna, P. W. M. Blom, F. Torricelli, *Nat. Commun.* **2020**, *11*, 3743.
[54] C.-Y. Yang, M.-A. Stoeckel, T.-P. Ruoko, H.-Y. Wu, X. Liu, N. B. Kolhe, Z. Wu, Y. Puttisong, C. Musumeci, M. Massetti, H. Sun, K. Xu, D. Tu, W. M. Chen, H. Y. Woo, M. Fahlman, S. A. Jenekhe, M. Berggren, S. Fabiano, *Nat. Commun.* **2021**, *12*, 2354.

[55] S. Cong, J. Chen, M. Xie, Z. Deng, C. Chen, R. Liu, J. Duan, X. Zhu, Z. Li, Y. Cheng, W. Huang, I. McCulloch, W. Yue, *Sci. Adv.* **2024**, *10*, eadq9405.
[56] T. Tan, X. Jiang, C. Wang, B. Yao, H. Zhang, *Adv. Sci.* **2020**, *7*, 2000058.
[57] D. A. Bernards, G. G. Malliaras, *Adv. Funct. Mater.* **2007**, *17*, 3538.
[58] P. Franceschini, A. Tognazzi, G. Finco, L. Carletti, I. Alessandri, A. C. Cino, C. D. Angelis, O. Takayama, R. Malureanu, A. V. Lavrinenko, D. de Ceglia, *Appl. Phys. Lett.* **2023**, *123*, 071701.
[59] A. Tognazzi, P. Franceschini, O. Sergaeva, L. Carletti, I. Alessandri, G. Finco, O. Takayama, R. Malureanu, A. V. Lavrinenko, A. C. Cino, D. de Ceglia, C. D. Angelis, *Adv. Photonics* **2023**, *5*, 066006.